Research Square

Preprints are preliminary reports that have not undergone peer review.
They should not be considered conclusive, used to inform clinical practice,
or referenced by the media as validated information.

# Stator Resistance Compensation for PI-Based Field-Oriented Control of SPMSM Drives Using a Multilevel Inverter

**Nguyen Vinh Quan**
Industrial University of Ho Chi Minh City
**Nguyen Ngoc Son**
nguyenngocson@iuh.edu.vn

Industrial University of Ho Chi Minh City

**Research Article**

**Keywords:** Surface permanent magnet synchronous motor (SPMSM), field-oriented control (FOC), PI control, stator resistance compensation, multilevel inverter, Hardware-in-the-Loop (HIL)

**Posted Date:** June 2nd, 2026

**DOI:** https://doi.org/10.21203/rs.3.rs-9591331/v1

**License:** This work is licensed under a Creative Commons Attribution 4.0 International License.
Read Full License

**Additional Declarations:** No competing interests reported.

# Stator Resistance Compensation for PI-Based Field-Oriented Control of SPMSM Drives Using a Multilevel Inverter

Nguyen Vinh Quan[1], Nguyen Ngoc Son[2]
[1,2]Faculty of Electronics Technology, Industrial University of Ho Chi Minh City, Ho Chi Minh City, Vietnam
Email: quan_01037027@iuh.edu.vn, nguyenngocson@iuh.edu.vn

**ABSTRACT.**

Field-Oriented Control (FOC) is widely used in high-performance Surface Permanent Magnet Synchronous Motor (SPMSM) drive systems due to its ability to achieve precise torque and current control. However, in practical applications, the stator resistance varies significantly with temperature, which introduces parameter mismatch in the d–q model and degrades the current tracking accuracy of conventional PI-based FOC designed with nominal parameters. This mismatch may reduce torque precision and weaken system robustness under load variations. To address this issue, this paper proposes a stator resistance compensation strategy integrated into the control voltage of the synchronous reference frame. The compensation term explicitly accounts for the stator resistance voltage drop, thereby improving the consistency between the control model and the actual motor characteristics under thermal variations. In addition, a multilevel voltage source inverter is employed to enhance output voltage quality and reduce current ripple and total harmonic distortion. The effectiveness of the proposed approach is verified through Lyapunov-based stability analysis, simulations, and FPGA-based Hardware-in-the-Loop (HIL) experiments. Results demonstrate improved current tracking performance, reduced steady-state error, and enhanced dynamic response for high-performance SPMSM drives.

**Keywords:** Surface permanent magnet synchronous motor (SPMSM), field-oriented control (FOC), PI control, stator resistance compensation, multilevel inverter, Hardware-in-the-Loop (HIL)

## I. Introduction

Permanent Magnet Synchronous Motors (PMSMs) have attracted increasing attention in industry due to the continuous development of their design technology and magnetic materials. In particular, PMSMs are expected to play an important role in the near future as the demand for electric vehicles continues to grow. PMSMs are approximately 15% more efficient than induction motors because of their high power density. In fact, it is predicted that more than 80% of electric vehicles will employ PMSMs in the near future [1].

Due to several notable advantages, including high power density, stable output torque, strong starting torque, long service life, high power factor, and good speed regulation capability [2], PMSMs can significantly improve the performance of electro-mechanical drive systems. Their high torque-to-inertia ratio and high efficiency make them an attractive replacement for induction motors in many industrial applications. For example, PMSMs can provide higher torque for the same motor size, while the motor size and weight can be reduced by nearly 25% for the same power rating. In addition, lower rotor losses contribute to efficiency improvements of up to 3%, while reduced motor noise enables smoother rotor operation. These advantages also help reduce the impact of torque ripple on motor bearings and improve the lifetime of the overall mechanical system [3]. Therefore, PMSMs have become a suitable choice in many applications, including electric vehicles and flight control systems [4].

Despite these advantages, improving the performance of PMSM drive systems still faces several persistent challenges, particularly at low speeds and under operating conditions where machine parameters vary due to temperature changes, load disturbances, and external uncertainties. These factors may degrade control accuracy and dynamic performance, making the design of robust control strategies an important research topic [5-8].

Among various control approaches, Field-Oriented Control (FOC) is one of the most widely adopted control strategies for PMSM drives. In typical implementations, FOC employs a multi-loop control architecture with PI controllers to regulate current and speed variables [9]. Although effective under nominal operating conditions, conventional PI-based FOC methods may experience performance degradation in the presence of parameter variations, load disturbances, and model uncertainties [10]–[11].

To address these limitations, various approaches have been investigated in the literature. These include the use of Kalman filtering techniques for accurate motor speed estimation [12], the application of real-

time evolutionary algorithms for parameter optimization [13], [14], electromagnetic torque compensation strategies for improved steady-state performance [15], and advanced harmonic injection methods for suppressing current harmonics [16]. Although these methods can improve certain aspects of system performance, they often suffer from limitations such as high computational complexity, limited adaptability to parameter variations, or reduced real-time performance in practical applications.

In addition, accurate rotor position information is essential for achieving high-performance closed-loop control in PMSM drives. In many existing systems, rotor position estimation is obtained using model-based observers such as flux observers [17], model reference adaptive systems (MRAS) [18], and sliding-mode observers (SMO) [19]. Among these approaches, SMO-based techniques are widely used due to their simple structure and strong robustness. However, inverter nonlinearities, switching dead-time, and other nonideal effects may cause deviations between the actual inverter output voltage and the reference voltage, which can introduce errors in rotor position estimation and degrade control performance [17]-[18].

Motivated by these challenges, this paper proposes a vector control scheme for the speed control of a Surface-mounted Permanent Magnet Synchronous Motor (SPMSM). The proposed algorithm is simple and easy to implement while improving the robustness of the drive system. In addition, a three-level voltage source inverter with delayed switching techniques is employed to reduce current and torque ripple and enhance the transient response of the system. The control structure consists of two PI control loops, including an inner current control loop and an outer speed control loop.

The main contributions of this paper are summarized as follows:

• A stator resistance compensation strategy is integrated into the PI-based Field-Oriented Control framework to mitigate parameter variations caused by temperature changes in SPMSM drives.

• A multilevel voltage source inverter is employed to improve output voltage quality and reduce current and torque ripple in the drive system.

• The proposed control scheme improves steady-state accuracy and robustness over a wide speed range (28–1500 rpm), which is validated through simulation and Hardware-in-the-Loop (HIL) experiments.

The remainder of this paper is organized as follows. Section 2 presents the mathematical model of the SPMSM and the multilevel inverter. Section 3 describes the proposed control strategy and the Lyapunov stability analysis. Section 4 presents simulation and HIL experimental results. Finally, Section 5 concludes the paper.

## II. Mathematical Model

### 2.1. PMSM model in the d–q reference frame

The mathematical model of a PMSM in an arbitrary rotating reference frame with angular speed $\omega_k$ can be expressed as shown in (1), where $\omega_r$ denotes the rotor angular speed and $\psi_f$ represents the permanent magnet flux linkage.

$$\begin{cases} \vec{u}_s = R_s \vec{i}_s + \dfrac{d\vec{\psi}_s}{dt} + j\omega_k \vec{\psi}_s,\ \vec{\psi}_s = L_s \vec{i}_s + \vec{\psi}_f \\ J\dfrac{d\omega_r}{dt} = (T_e - T_L) \end{cases} \quad (1)$$

For control design purposes, it is convenient to express the motor model in the synchronous rotating $d$-$q$ reference frame aligned with the rotor. In this reference frame, the dynamic behavior of the PMSM can be represented using the $d$-axis and $q$-axis voltage equations. The equivalent representation of the PMSM in the $d$-$q$ frame is illustrated in Fig. 1. In this model, the stator flux linkage is composed of two components, including the flux generated by the stator currents and the flux produced by the permanent magnets.

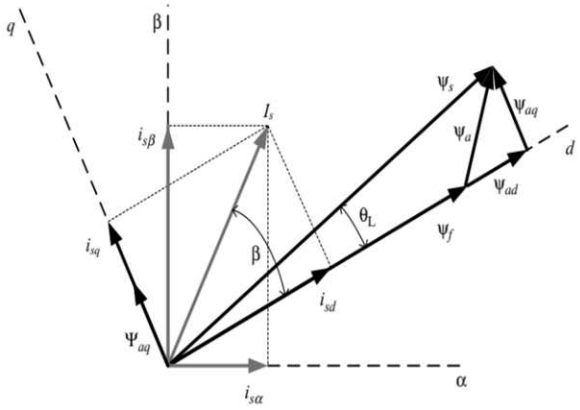



*Figure 1. Phasor diagram of the stator flux and stator current*

In PMSMs, the main magnetic field is produced by permanent magnets; therefore, the rotor flux linkage can be considered constant over time. The mathematical model of the PMSM in the synchronous rotating $d$-$q$ reference frame aligned with the rotor can be expressed in terms of the state-variable differential equations as follows.

The stator current equations are given by

$$\begin{cases} \dfrac{di_d}{dt} = -\dfrac{R_s}{L_d} i_d + \dfrac{L_q}{L_d} p\omega_r i_q + \dfrac{1}{L_d} u_d \\ \dfrac{di_q}{dt} = -\dfrac{R_s}{L_q} i_q - \dfrac{L_d}{L_q} p\omega_r i_d - \dfrac{1}{L_q} p\omega_r \psi_f + \dfrac{1}{L_q} u_q \end{cases} \quad (2)$$

The mechanical dynamics of the rotor can be expressed as

$$\begin{cases} \frac{d\omega_r}{dt} = \frac{1}{J}(T_e - T_L - B\omega_r) \\ \frac{d\theta_r}{dt} = \omega_r \end{cases} \quad (3)$$

The electromagnetic torque produced by the PMSM is given by

$$T_e = \frac{3}{2}p\left[\psi_f i_q + i_d i_q \left(L_d - L_q\right)\right] \quad (4)$$

For a surface-mounted permanent magnet synchronous motor (SPMSM), which is a non-salient pole machine, the inductances of the $d$-axis and $q$-axis are equal $\left(L_d = L_q = L_s\right)$. Therefore, the torque equation can be simplified as

$$T_e = \frac{3}{2}p\,\psi_f i_q \quad (5)$$

where $\psi_f$ is the permanent magnet flux linkage, $p$ is the number of pole pairs, $v_d$ and $v_q$ are the stator voltages in the $d$- and $q$-axes, and $i_d$ and $i_q$ denote the stator currents. $R_s$ is the stator resistance, while $L_d$ and $L_q$ are the stator inductances along the $d$- and $q$-axes, respectively. Furthermore, $\omega_r$ is the rotor angular speed, $J$ is the rotor inertia, $T_L$ is the load torque, $T_e$ is the electromagnetic torque, $B$ is the viscous friction coefficient, and $\theta_r$ represents the rotor angular position.

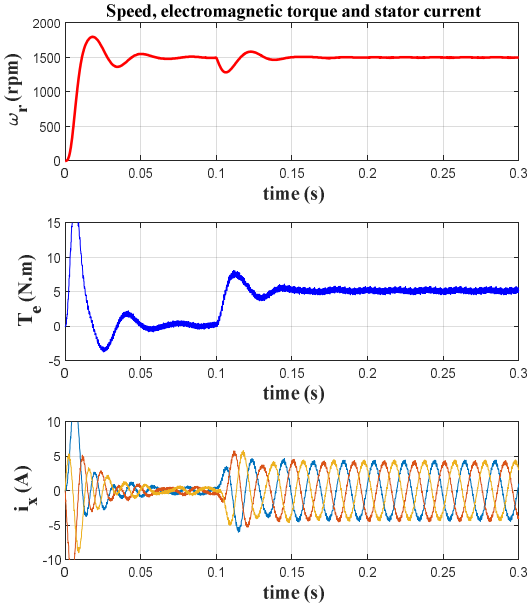



*Figure 2. Simulated waveforms for motor free acceleration of PMSM.*

To illustrate the dynamic characteristics of the PMSM model, a free-acceleration simulation is performed. Fig. 2 shows the rotor speed $\omega_r$, electromagnetic torque $T_e$, and stator phase currents $i_x$ $(x = a, b, c)$ when the motor starts under rated voltage and frequency without mechanical load.

The starting current reaches approximately 10 A, enabling the rotor speed to reach its rated value of 1500 rpm within about 0.1 s due to the low inertia. A transient increase in torque around 0.1 s causes a current overshoot exceeding 5 A and a short oscillation in speed. After a brief transient, the rotor speed stabilizes at the rated value while the stator current decreases below 5 A.

**2.2 Effect of stator resistance on FOC performance**

In PMSMs, the main excitation field is generated by permanent magnets mounted on the rotor. Ideally, the rotor flux linkage $\psi_f$ can be considered constant over time. Therefore, in FOC, the electromagnetic torque can be regulated by controlling the q-axis current $i_q$, while the d-axis current $i_d$ is maintained at zero in the constant torque region below the base speed.

However, in practical PMSMs, the total air-gap flux is composed of both the permanent magnet flux and the stator reaction flux

$$\vec{\psi}_{total} = \vec{\psi}_f + \vec{\psi}_{stator} \quad (6)$$

where $\psi_{stator}$ represents the armature reaction flux generated by the stator current. The interaction between these flux components is referred to as the armature reaction effect. As a result, when $i_d > 0$, the total flux increases, whereas when $i_d < 0$, the total flux decreases, which corresponds to the flux-weakening operation.

For SPMSMs, since $L_d \approx L_q$, the electromagnetic torque mainly depends on the q-axis current, whereas the d-axis current primarily influences the magnitude of the air-gap flux. In addition, the armature reaction caused by the stator current may distort the air-gap flux distribution and lead to localized magnetic saturation, thereby affecting the effective inductance parameters of the motor.

Another important factor affecting the performance of FOC is the variation of stator resistance with temperature. The stator resistance can be expressed as

$$R_s(T) = R_{so}[1 + \alpha\left(T - T_o\right) \quad (7)$$

where $R_{s0}$ is the stator resistance measured at the reference temperature $T_0$ (typically between 20 °C and 25°C), and $\alpha$ is the temperature coefficient of resistance, which is approximately $\alpha \approx 0.0039$ /°C (Cu) for copper windings.

When the stator resistance $R_s$ increases due to temperature variation, the voltage drops $R_s i_d$ and $R_s i_q$ increase correspondingly. As a result, operating-point drift, torque deviation, efficiency reduction, and speed oscillations may occur. Moreover, if the $i_d$ current becomes uncontrolled, there exists a potential risk of permanent magnet demagnetization.

**2.3 PI control law**

Fig. 3 shows the typical block diagram of vector control for a permanent magnet synchronous motor (PMSM) in

the synchronous d–q reference frame. This control structure allows the PMSM to be handled similarly to a separately excited DC motor. The control system consists of the PMSM model and the d–q axis control loops connected to the rotor speed control loop. In this scheme, PI controllers are commonly used to regulate the motor speed and current components.

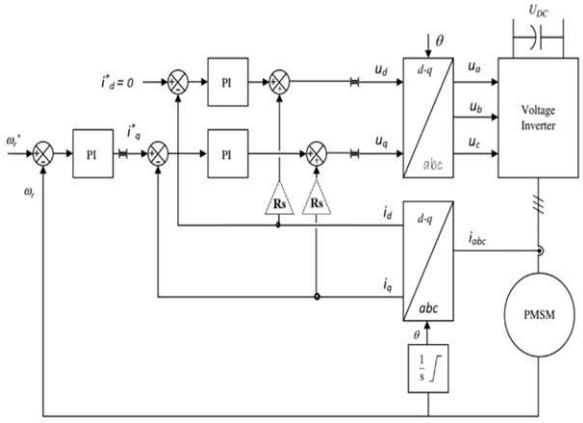



*Fig. 3. Vector control scheme of permanent magnet synchronous machine*

Maintaining $i_d = 0$ is the most common control strategy for PMSMs, since it helps protect the machine from over-excitation or under-excitation conditions. The PI controller for the d-axis generates the control voltage $u_d$, while the rotor speed controller determines the reference q-axis current $i_q^*$, which in turn produces the q-axis voltage component $u_q$.

In PMSMs, the main magnetic field is generated by permanent magnets mounted on the rotor. Ideally, the flux linkage is constant over time. However, in practice, the stator current produces its own magnetic field, which interacts with the original field and causes the armature reaction effect. As indicated in (2), the currents $i_d$ and $i_q$ are influenced by the stator resistance $R_s$, especially when temperature variations occur. Therefore, reducing the influence of this parameter variation is necessary. The rotor position is given by:

$$\theta_r = \int \omega_r dt \tag{8}$$

The stator voltages and currents are then transformed into two-phase variables through forward and inverse transformation blocks. The corresponding relations are expressed as

$$\begin{bmatrix} d \\ q \\ 0 \end{bmatrix} = \frac{2}{3} \begin{bmatrix} \sin(\theta) & \sin(\theta - \frac{2\pi}{3}) & \sin(\theta + \frac{2\pi}{3}) \\ \cos(\theta) & \cos(\theta - \frac{2\pi}{3}) & \cos(\theta + \frac{2\pi}{3}) \\ \frac{1}{2} & \frac{1}{2} & \frac{1}{2} \end{bmatrix} \begin{bmatrix} a \\ b \\ c \end{bmatrix} \tag{9}$$

$$\begin{bmatrix} a \\ b \\ c \end{bmatrix} = \begin{bmatrix} \sin(\theta) & \cos(\theta) & 1 \\ \sin(\theta - \frac{2\pi}{3}) & \cos(\theta - \frac{2\pi}{3}) & 1 \\ \sin(\theta + \frac{2\pi}{3}) & \cos(\theta + \frac{2\pi}{3}) & 1 \end{bmatrix} \begin{bmatrix} d \\ q \\ 0 \end{bmatrix} \tag{10}$$

From the system equations in (2), if $u_d$ and $u_q$ are selected as the control inputs for $i_d$ and $i_q$, respectively, the control laws can be designed as

$$u_d = R_s i_d + K_{dp} e_d + K_{di} \int e_d dt \tag{11}$$

$$u_q = R_s i_q + K_{qp} e_q + K_{qi} \int e_q dt \tag{12}$$

$$i_q^* = K_{\omega p} e_\omega + K_{\omega i} \int e_\omega dt \tag{13}$$

where the control errors are defined as $e_d = i_d^* - i_d$, $e_q = i_q^* - i_q$, and $e_\omega = \omega_r^* - \omega_r$. The parameters $K_{dp}, K_{di}, K_{qp}, K_{qi}, K_{\omega p}, K_{\omega i}$ denote the PI controller gains, while $i_d, i_q, \omega_r$ are the measured variables.

Substituting (11) and (12) into (2), it can be observed that the terms $R_s i_d$ and $R_s i_q$ are eliminated. Therefore, the currents $i_d$ and $i_q$ are no longer affected by variations in the stator resistance $R_s$ due to temperature changes, which demonstrates the robustness of the proposed control law.

$$\begin{cases} L_s \frac{di_d}{dt} = L_s p \omega_r i_q + K_{dp} e_d + K_{di} \int e_d dt \\ L_s \frac{di_q}{dt} = -L_s p \omega_r i_d - p \omega_r \psi_f + K_{qp} e_q + K_{qi} \int e_q dt \end{cases} \tag{14}$$

**2.4 Lyapunov stability analysis**

Since $i_d = i_d^* - e_d$ and $i_q = i_q^* - e_q$, where $i_d^*$ and $i_q^*$ are constant reference values, their derivatives satisfy $\dot{e}_d = -\dot{i}_d, \dot{e}_q = -\dot{i}_q$

Let:

$$\begin{cases} \eta_d = \int e_d dt, \ \eta_q = \int e_q dt \\ \dot{\eta}_d = e_d, \ \dot{\eta}_q = e_q \end{cases} \tag{15}$$

Substituting (15) into (14) yields

$$\begin{cases} L_s \dot{e}_d = -L_s p \omega_r \left( i_q^* - e_q \right) - K_{dp} e_d - K_{di} \eta_d \\ L_s \dot{e}_q = L_s p \omega_r \left( i_d^* - e_d \right) + p \omega_r \psi_f - K_{qp} e_q - K_{qi} \eta_q \end{cases} \tag{16}$$

Let:

$$\begin{cases} C_d = -L_s p \omega_r i_q^* \\ C_q = L_s p \omega_r i_d^* + p \omega_r \psi_f \end{cases} \tag{17}$$

Substituting (17) into (16), we obtain

$$\begin{cases} L_s \dot{e}_d = L_s p \omega_r e_q - K_{dp} e_d - K_{di} \eta_d + C_d \\ L_s \dot{e}_q = -L_s p \omega_r e_d - K_{qp} e_q - K_{qi} \eta_q + C_q \end{cases} \tag{18}$$

At the desired equilibrium point $e_d = e_q = 0$, the conditions $C_d = C_q = 0$ must be satisfied. Therefore, the deviation around the equilibrium point is expressed

as

$$\begin{cases} L_s \dot{e}_d = L_s p \omega_r e_q - K_{dp} e_d - K_{di} \eta_d \\ L_s \dot{e}_q = -L_s p \omega_r e_d - K_{qp} e_q - K_{qi} \eta_q \end{cases} \quad (19)$$

To analyze the stability of the system, consider the Lyapunov function candidate $V$, which satisfies $V > 0$ for all $x \neq 0$

$$V = \frac{1}{2} L_s \left( e_d^2 + e_q^2 \right) + \frac{1}{2} K_{di} \eta_d^2 + \frac{1}{2} K_{qi} \eta_q^2 \quad (20)$$

The time derivative of the Lyapunov function is given by

$$\dot{V} = L_s \dot{e}_d e_d + L_s \dot{e}_q e_q + K_{di} \eta_d e_d + K_{qi} \eta_q e_q \quad (21)$$

Substituting (18) into (21), we obtain

$$\dot{V} = - K_{dp} e_d^2 - K_{qp} e_q^2 \quad (22)$$

Therefore, if the controller gains satisfy $K_{dp} > 0$ and $K_{qp} > 0$, the control laws defined in (11)–(12) ensure global asymptotic stability of the system.

**2.5. Inverter and hysteresis switching**

Fig. 4 shows the three-level diode-neutral-point-clamped (D-NPC) voltage source inverter supplying the PMSM. The inverter consists of four switches $S_1$–$S_4$ with antiparallel diodes $D_1$–$D_4$, typically implemented using IGBTs or GCTs.

Two DC-link capacitors $C_{d1}$ and $C_{d2}$ form the neutral point $Z$, while $D_{Z1}$ and $D_{Z2}$ act as clamping diodes. When $S_2$ and $S_3$ are ON, the inverter output is connected to the neutral point. Each capacitor voltage is $E = V_d/2$. Due to the neutral current $i_Z$, capacitor charging and discharging may cause neutral-point voltage imbalance.

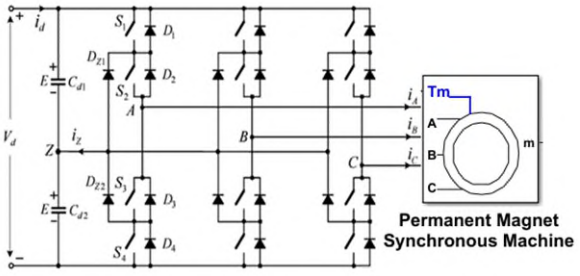



*Fig. 4. Structure of the three-level inverter supplying the PMSM.*

The inverter produces three output voltage levels as $+V_d/2$, $-V_d/2$ and 0 with complementary switching states $S_1 + S_3 = 1 \; and \; S_2 + S_4 = 1$.

The switching signals are generated by comparing the stator voltage $u_x$ with a hysteresis band $h$. A double-band hysteresis scheme (Fig. 5) produces three outputs $y = +1, 0, -1$, corresponding to acceleration, deceleration, and no change in rotor speed.

$$S_1 = \begin{cases} 1 & \text{if } u_x > +h \\ 0 & \text{Otherwise} \end{cases} \qquad S_2 = \begin{cases} 1 & \text{if } u_x > -h \\ 0 & \text{Otherwise} \end{cases}$$

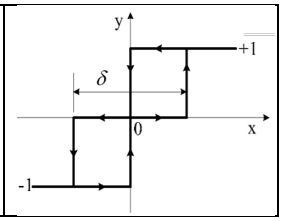



*Fig. 5. Characteristics of hysteresis*

Switching occurs between $S_1$–$S_3$ when $u_x > 0$, and between $S_2$–$S_4$ when $u_x < 0$. This scheme distributes switching losses among devices within one cycle. Fig. 6 shows the influence of the hysteresis band $h$and frequency $f$on the stator current THD, defined as

$$\text{THD}(h, f) = \frac{\sqrt{\sum_{n=2}^{\infty} I_n^2 (h, f)}}{I_1} \times 100\% \quad (23)$$

Increasing $h$ enlarges current ripple and increases THD, whereas higher frequency $f$ generally reduces THD but increases switching losses. Therefore, an optimal compromise between current quality and switching loss must be considered.

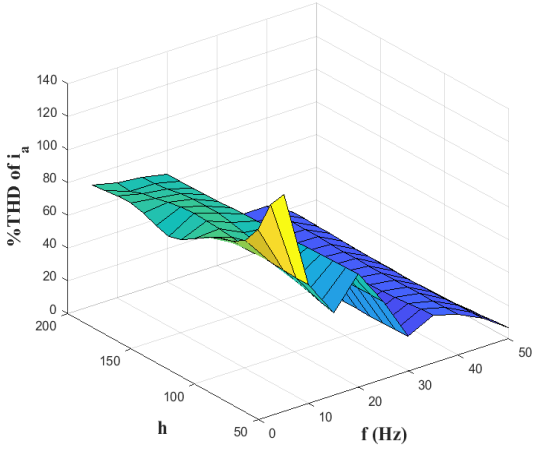



Fig. 6. Effect of $h$and $f$on stator current THD.

**2.6. Hardware in the loop design**

FPGA provides significant advantages for high-performance SPMSM drive systems due to its true parallel processing capability. Unlike DSP-based controllers that operate sequentially, FPGA allows Clarke/Park transformations, current control, decoupling, and modulation algorithms to be executed simultaneously within the same sampling period, thereby reducing computational delay [20-22].

Hardware-in-the-loop (HIL) techniques have gained increasing attention in power electronics and drive systems as a fast and reliable approach for validating control strategies. HIL platforms allow real-time evaluation of controller performance before practical implementation, thereby reducing development risk, cost, and time [23-24].

To accurately emulate the inverter behavior, the HIL system must reproduce the VSI characteristics

with sampling times typically in the range of 10–50 µs. This requirement can be achieved using the time-stamping bridge technique.

In this study, the average model of the D-NPC inverter and the SPMSM is implemented on a PC, while the control algorithm is deployed on an FPGA, forming a complete HIL system. The FPGA generates the switching states $S_{jx}$ of the multilevel inverter, which are transmitted to the PC where the inverter and SPMSM average models are simulated. Feedback signals, including stator currents and rotor speed, are sent back to the FPGA to close the real-time control loop, while the electromagnetic torque $T_e$ is estimated on the PC.

### 2.7. Average model of VSI and SPMSM

The average model of the three-level D-NPC inverter supplying the stator voltage of the SPMSM is expressed as

$$\bar{u}_x = \frac{V_d}{2}\left(\sum_{j=1,2} S_{jx}\right) \tag{24}$$

where $\bar{u}_x$ represents the three-phase inverter output voltages and $S_{jx}$ denotes the switching states.

In the rotating $d$-$q$ reference frame, the average voltage model of the SPMSM can be written as

$$\begin{cases} \bar{u}_d = R_s i_d + L_s \dfrac{di_d}{dt} - L_s p\omega_r i_q \\ \bar{u}_q = R_s i_q + L_s \dfrac{di_q}{dt} + p\omega_r \left(L_s i_d + \psi_f\right) \end{cases} \tag{25}$$

Note that the inverter output voltage $\bar{u}_x$ given in (24) accurately represents the practical inverter behavior, including switching actions and high-frequency ripple.

## III. Simulation and experimental results

Simulation and experimental studies were carried out in MATLAB/Simulink with a simulation time of $T_{stop} = 7\ s$. The parameters of the SPMSM are listed in Table 1. During the test, the reference speed $\omega_r^*$ varies from 28 rpm to 1500 rpm.

**Table 1.** SPMSM parameters

| Parameter | Value | Unit |
|---|---|---|
| Power | 1, 380, 50 | hp, V, Hz |
| Velocity of the rotor | $\omega_r = 1500$ | rpm |
| Electromagnetic torque | $T_e = 4.75$ | N.m |
| Resistance of the stator | $R_s = 2.875$ | Ω |
| $dq$-axis inductances $L_{dq}$ | $L_d = L_q = 8.5$ | mH |
| Number of pole pairs | $p = 2$ | |
| Combined inertia of rotor and load | $J = 0.8e\text{-}3$ | kg.m$^2$ |
| Combined viscous friction of rotor and load | $F = 1e\text{-}3$ | N.m.s |
| Amplitude of rotor PM-induced flux in the stator | $\psi_f = 0.25$ | V.s |
| Time sampling | $T_s = 10$ | µs |
| $V_{dc}$ Link | $V_{dc} = 400$ | V |

The objective is to develop a robust PMSM speed controller capable of maintaining high dynamic performance around the operating point, particularly under load variations and input voltage changes. The controller aims to achieve limited overshoot, short settling time, and reduced output harmonics while preserving consistent dynamic performance under different operating conditions.

The system performance is evaluated under three scenarios: variation of the reference speed $\omega_r^*$, variation of motor parameters, and the presence of unknown disturbances, including random disturbances $d(t)$.

### 3.1 Simulation Results

Fig. 7 shows the inverter output characteristics. The DC-link capacitor voltages are balanced at $V_{dc}/2 = 200$ V. The phase voltage $V_{an}$ exhibits three distinct levels $(-V_{dc}/2, 0, +V_{dc}/2)$ as shown in Fig. 7(a), while the line voltage $V_{ab}$ presents five levels ranging from $-V_{dc}$ to $+V_{dc}$.

The common-mode voltage is reduced to $V_{dc}/6$. The stator current has a fundamental component of 50 Hz with an amplitude of approximately 4.9 A, and its total harmonic distortion (THD) is around 8%, as illustrated in Fig. 7(b).

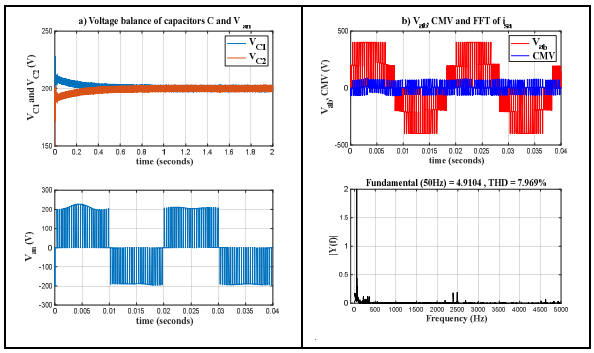



*Fig. 7. D-NPC inverter response.*

Fig. 8 shows the rotor speed response and tracking performance. The red curve represents the reference speed, while the dashed blue curve denotes the measured speed. The results indicate that, after the acceleration phase, the measured speed closely follows the reference with a settling time of approximately 0.1 seconds.

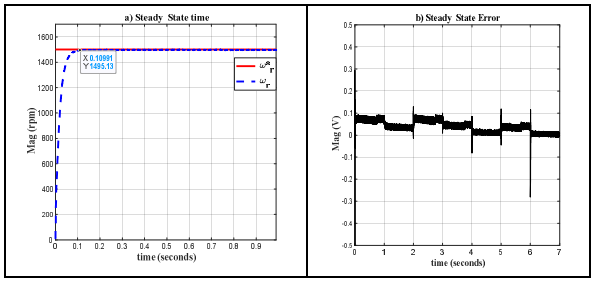



*Fig. 8. Settling time and error of rotor speed $\omega_r$*

Fig. 9 shows that the measured rotor speed $\omega_r$ and electromagnetic torque $T_e$ closely track their reference values $\omega_r^*$ and $T_e^*$, respectively. The q-axis current $i_q$ varies with the reference speed to maintain the required torque.

At low speed (28 rpm), the stator current reaches approximately 4 A, indicating that the controller increases its control effort to ensure robust performance under low-speed operating conditions.

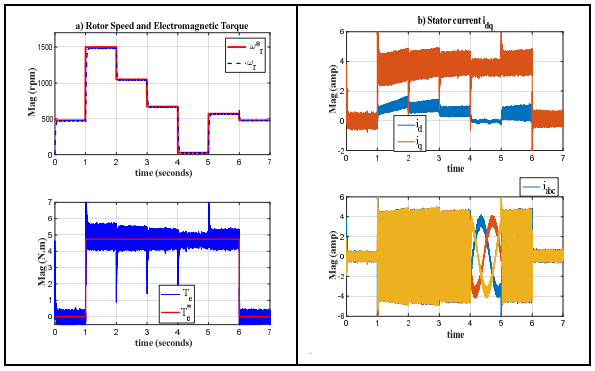



*Fig. 9. SPMSM response at $T_e = 4.75\ N.m$*

Fig. 10 shows the SPMSM response under varying load torque. The rotor speed and electromagnetic torque accurately track their reference values. The q-axis current $i_q$ varies according to the speed and torque demands. During the interval from 4 to 5 s, when the speed reaches its minimum and the torque reaches its maximum, the stator current exceeds 4 A.

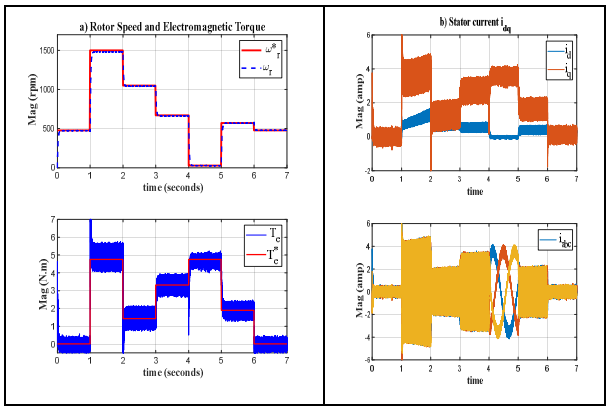



*Fig. 10. SPMSM response under varying torque.*

To evaluate the impact of parameter variations on system performance, the stator resistance $R_s$ is increased to twice its nominal value, together with the presence of random disturbances.

Fig. 11 shows the system response when the stator resistance $R_s$ is doubled and the torque $T_e$ varies. The measured variables still track their references accurately. The stator current exceeds 4 A at low speed while maintaining a sinusoidal waveform, prove that the control laws in (11)–(12) are robust against variations in $R_s$.

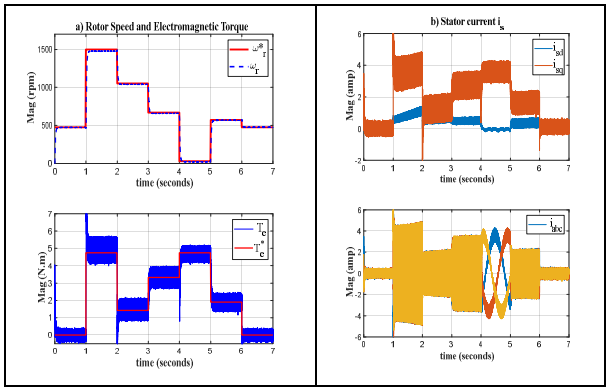



*Fig. 11. SPMSM response with doubled $R_s$*

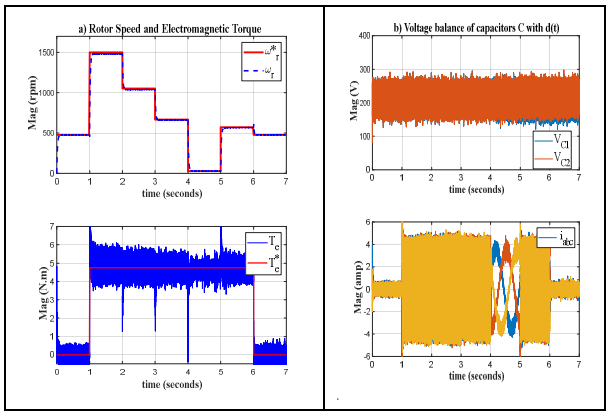



*Fig. 12. SPMSM response under disturbance $d(t)$.*

Fig. 12 presents the system performance under random disturbances $d(t)$ with an amplitude of ±70 V applied to the DC-link voltage. The measured speed and torque continue to follow their references. During the interval from 2 to 3 s, slight torque oscillations are observed at higher speeds. The DC-link capacitor voltages are rebalanced to a new value, and the stator current remains sinusoidal, exceeding 4 A at low speed.

Overall, the simulation results indicate that the decoupled control of the d- and q-axis currents simplifies the control design and improves accuracy. In addition, the multilevel structure of the VSI provides clearly defined voltage levels, contributing to improved system performance and robustness.

Fig. 13 illustrates the stator current trajectory in the stationary $\alpha\beta$ frame. The current components $i_\alpha$ and $i_\beta$, obtained via Clarke transformation, form nearly circular trajectories, indicating that the magnitude of the stator current vector is well regulated. This confirms the effective decoupling of $i_d$ and $i_q$, where $i_d \approx 0$ and $i_q$ is responsible for torque generation.

The slight deviation from an ideal circular trajectory can be attributed to inverter switching effects, sampling errors, and current ripple components. The irregular behavior near the center reflects the transient phase during the transition from startup to

steady-state operation. Once steady state is reached, the stator current vector rotates uniformly in the $\alpha\beta$ plane, forming a nearly circular trajectory with an approximately constant radius.

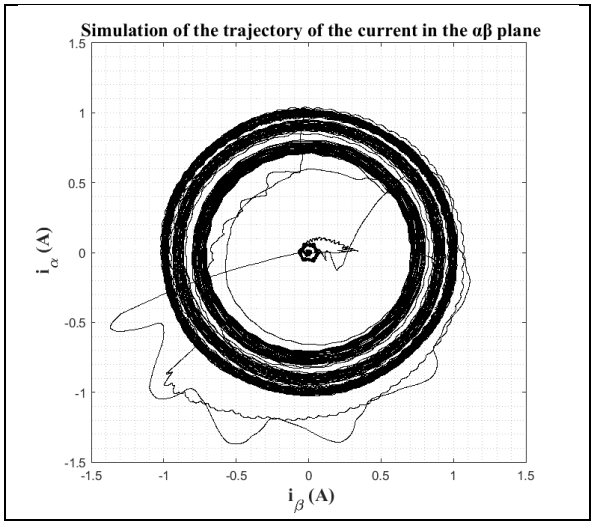



*Fig. 13. Stator current trajectory in the stationary $\alpha\beta$ frame under FOC.*

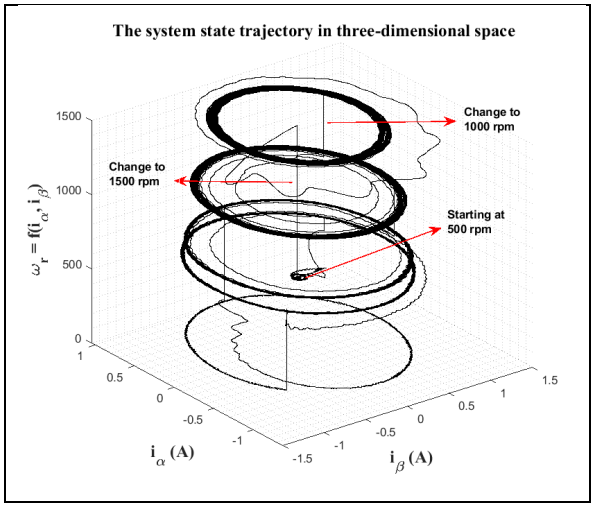



*Fig. 14. Three-dimensional trajectory of the system states* ($i_\alpha$, $i_\beta$, $\omega_r$)

Fig. 14 illustrates the three-dimensional trajectory of the stator current in the stationary $\alpha\beta$frame combined with the rotor speed $\omega_r$. The horizontal axes represent $i_\alpha$and $i_\beta$, while the vertical axis corresponds to $\omega_r$. At each speed level, the stator current trajectory in the $\alpha\beta$ plane forms an approximately circular shape, indicating that the magnitude of the current vector is well maintained under FOC. The vertical displacement of these trajectories reflects the variation of rotor speed during transient and steady-state operation.

The patterns represent the transient response as the speed changes (e.g., from 500 rpm to 1500 rpm and 1000 rpm), forming spiral trajectories along the $\omega_r$ axis. Once steady state is reached, the stator current remains sinusoidal with nearly constant amplitude for different speed levels, as expressed in (26).

$$\left|\vec{i}_s\right| = \sqrt{i_\alpha^2 + i_\beta^2} \approx \text{constant} \tag{26}$$

### 3.2 Experimental Results

Fig. 15 shows the real-time experimental setup of the proposed control scheme. The rotor speed is measured using a 1024-pulse encoder, and the data are acquired on a PC.

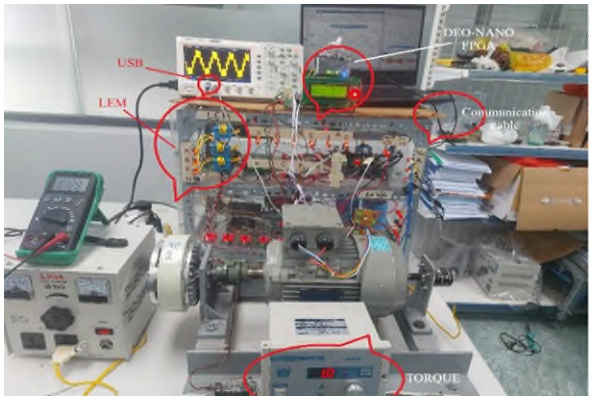



*Fig. 15. Experimental setup.*

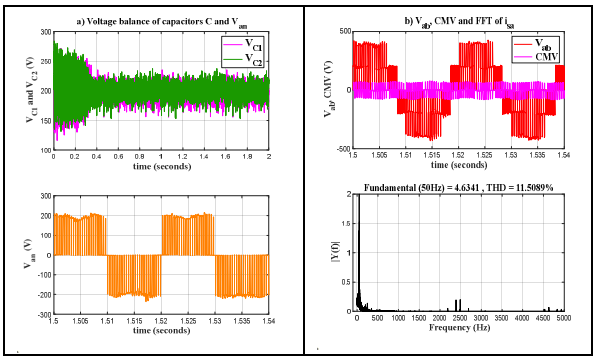



*Fig. 16. Experimental D-NPC response.*

Fig. 16 presents the experimental inverter performance. The DC-link capacitor voltages are balanced at $V_{dc}/2 = 200\,\text{V}$, and the phase voltage exhibits three distinct levels. The common-mode voltage is reduced to $V_{dc}/6$. The stator current has a fundamental component of 50 Hz with an amplitude of approximately 4.6 A, and the THD is around 11.5%.

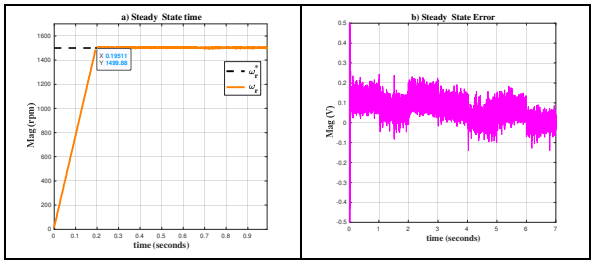



*Fig. 17. Settling time and error of rotor speed*

Fig. 17 shows the experimental rotor speed response. The dashed black curve represents the reference speed, while the orange curve denotes the measured speed. The results indicate fast acceleration and accurate tracking, with a settling time of

approximately 0.2 s. The longer settling time compared to the simulation results is mainly due to sampling delay $t_d$ between the FPGA and the proposed models.

Fig. 18 shows the experimental results at $T_e = 4.75$ N.m. The measured rotor speed $\omega_r$ and torque $T_e$ (dashed lines) closely track their reference values $\omega_r^*$and $T_e^*$ (solid lines). The q-axis current $i_q$varies with the speed reference to maintain the required torque. At low speed (28 rpm), the stator current reaches approximately 5 A while maintaining a sinusoidal waveform.

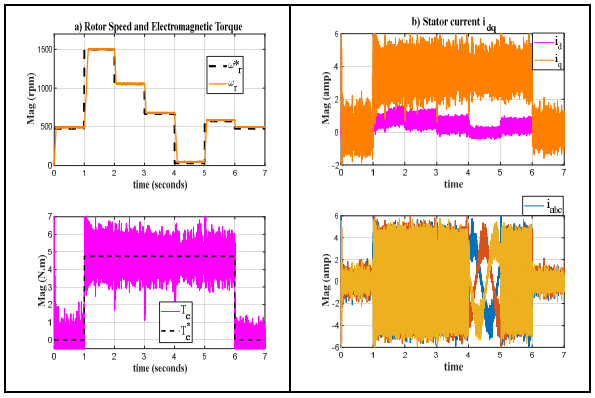



*Fig. 18. Experimental response at rated $T_e$*

Fig. 19 shows the experimental response under varying torque conditions. The measured variables closely track their reference values. During the interval from 2 to 3 s, higher speed operation leads to noticeable oscillations in the q-axis current $i_q$, which continuously adapts to the speed reference while maintaining torque variation. At the highest speed, the stator current reaches approximately 6 A and retains a sinusoidal waveform.

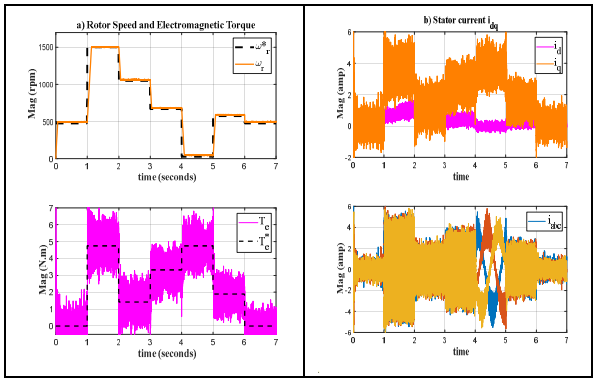



*Fig. 19. Experimental response under varying $T_e$*

Fig. 20 shows the experimental results when the stator resistance $R_s$ is doubled and the torque $T_e$ varies. The measured variables still track their references accurately. At the highest speed, the stator current reaches approximately 6 A while maintaining a sinusoidal waveform, and the q-axis current increases to meet the speed demand. These results confirm that the proposed control law is largely independent of $R_s$, consistent with the simulation results.

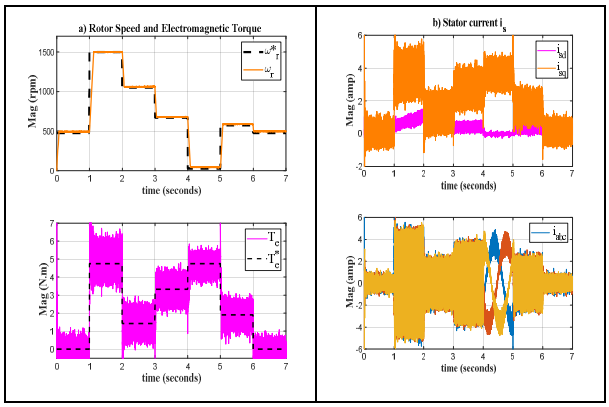



*Fig. 20. SPMSM response with doubled $R_s$.*

Fig. 21 presents the system performance under disturbances $d(t)$. The measured variables continue to follow their references. At higher speeds, slight torque oscillations are observed, while the DC-link capacitor voltages are rebalanced to a new level. The stator current exceeds 4 A at low speed and retains a sinusoidal waveform.

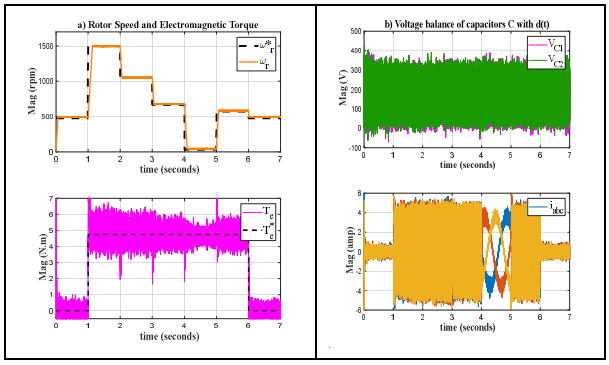



*Fig. 21. Experimental response under disturbance d(t)*

Figs. 22 and 23 illustrate the experimental stator current trajectory in the $\alpha\beta$ plane and the state trajectory in the three-dimensional space $(i_\alpha, i_\beta, \omega_r)$, respectively. The results show that the stator current maintains a sinusoidal waveform with stable amplitude, confirming the dynamic stability of the SPMSM drive under the FOC scheme.

Where, Fig. 22 shows that the stator current vector forms nearly circular trajectories as the system approaches steady state. The spiral trajectory from the origin reflects the transient phase during startup, where the current magnitude gradually increases. Once steady state is reached, the current vector rotates uniformly with an approximately constant radius.

In Fig. 23, the experimental state trajectory in the three-dimensional space, where the vertical axis represents the rotor speed. The circular stator current trajectories in the $\alpha\beta$plane are lifted along the speed axis, forming layered trajectories at different speed levels. This behavior reflects the evolution of the system from the startup phase to steady-state operation.

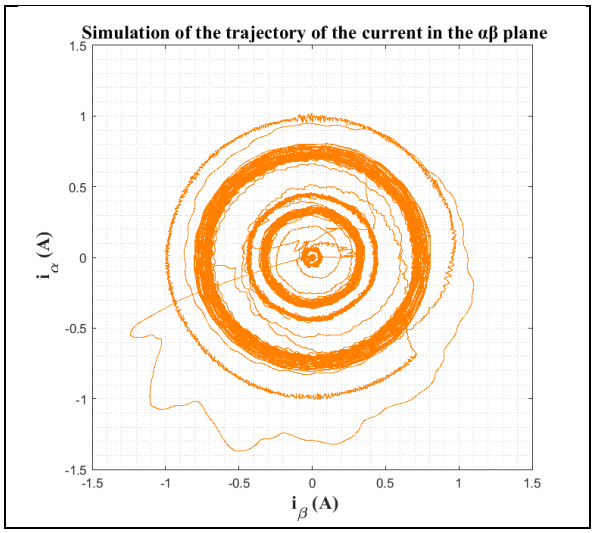



*Fig. 22. Trajectory of the stator current vector in the αβ frame under FOC of the SPMSM*

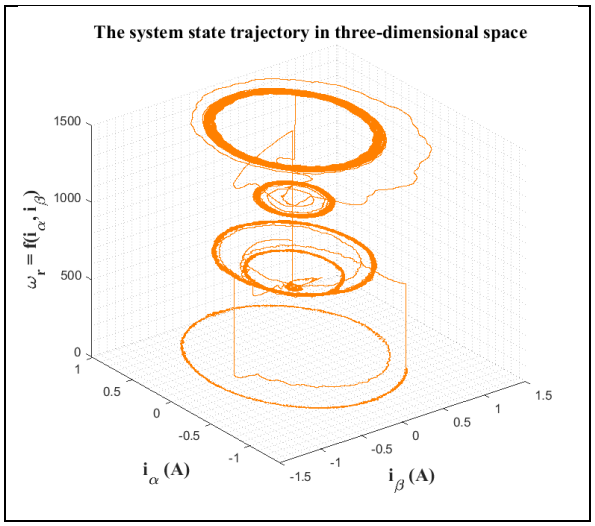



*Fig. 23. Three-dimensional trajectory of the system states ($i_\alpha$, $i_\beta$, $\omega_r$)*

## IV. Conclusions

This paper has presented a PI-based field-oriented control strategy for SPMSM drives with integrated stator resistance compensation and a multilevel inverter employing hysteresis switching. The proposed method effectively mitigates the impact of parameter variations, particularly stator resistance changes due to temperature. The robustness of the control scheme has been validated under parameter variations and external disturbances. Both simulation and real-time experimental results demonstrate improved current tracking, reduced harmonic distortion, and enhanced dynamic performance, especially under low-speed and load-varying conditions. Furthermore, the use of a multilevel inverter contributes to improved voltage quality and reduced current ripple, leading to better overall system performance. The results confirm that the proposed approach provides a simple, effective, and practically applicable solution for high-performance SPMSM drive systems.

**Conflicts of Interest**. The authors declare no competing interests.

**Contributions**. PhD. Nguyen Vinh Quan and Assoc. Prof. Nguyen Ngoc Son worked together to design the study, collect and analyze the data, and write the first draft of the paper. All authors read and approved the final manuscript.

**Funding**: Not applicable

## References

[1]. R. Dermouche, M. Tadjine, A. Talaoubrid, M. Fazilat, N. Zioui, "A quantum direct torque control method for permanent magnet synchronous machines," *Computers and Electrical Engineering*, vol. 122, p. 109994, 2025. **DOI:** 10.1016/j.compeleceng.2024.109994

[2]. W. Sun, H. Si, J. Qiu, J. Li, "Research on efficiency of permanent-magnet synchronous motor based on adaptive algorithm of fuzzy control," *Sustainability*, vol. 16, no. 3, p. 1253, 2024. **DOI:** 10.3390/su16031253

[3]. Q. Huang, Q. Huang, H. Guo, J. Cao, "Design and research of permanent magnet synchronous motor controller for electric vehicle," *Energy Science & Engineering*, vol. 11, no. 1, pp. 112–126, 2023. **DOI:** 10.1002/ese3.1316

[4]. D. Karboua, B. Toual, A. Kouzou, B. O. Douara, T. Mebkhouta, A. N. Bendenidina, "High-order super-twisting based terminal sliding mode control applied on three phases permanent synchronous machine," *Periodica Polytechnica Electrical Engineering and Computer Science*, vol. 67, no. 1, pp. 40–50, 2023. **DOI:** 10.3311/PPee.21026

[5]. X. Zhang, S. Fang, H. Zhang, "Predictive current error compensation-based strong robust model predictive control for PMSM drive systems," *IEEE Transactions on Industrial Electronics*, vol. 71, no. 12, pp. 15280 - 15289,

2024. **DOI:** 10.1109/TIE.2024.3379650

[6]. S. Liu, Z. Song, Y. Liu, Y. Chen, C. Liu, "Flux-weakening controller design of dual three-phase PMSM drive system with copper loss minimization," *IEEE Transactions on Power Electronics*, vol. 38, no. 2, pp. 2351–2363, 2023, **DOI:** 10.1109/TPEL.2022.3216513

**[7].** Z. Sun, Y. Deng, J. Wang, T. Yang, Z. Wei, H. Cao, "Finite control set model-free predictive current control of PMSM with two voltage vectors based on ultralocal model," *IEEE Transactions on Power Electronics*, vol. 38, no. 1, pp. 776–788, 2023, **DOI**: 10.1109/TPEL.2022.3198990.

[8]. S. Xu, Q. He, S. Tao, H. Chen, Y. Chai, W. Zheng, "Pig face recognition based on trapezoid normalized pixel difference feature and trimmed mean attention mechanism," *IEEE Transactions on Instrumentation and Measurement*, vol. 72, pp. 3500713, 2022, **DOI**: 10.1109/TIM.2022.3232093.

[9]. R. G. Shriwastava, S. S. Kadlag, J. G. Chaudhari, P. R. Sonawane, N. Dhote, "A multi-level neutral-point-clamped inverter driven PMSM high-speed electric drive," *International Journal of Electric and Hybrid Vehicles*, vol. 16, no. 1, 2024, **DOI**: 10.1504/IJEHV.2024.140015

[10]. Z. Novak, "Confidence weighted learning entropy for fault-tolerant control of a PMSM with a high-resolution hall encoder," *IEEE Transactions on Industrial Electronics*, vol. 71, no. 5, pp. 5176–5186, 2024. **DOI:** 10.1109/TIE.2023.3283690

[11]. A. Aboelhassan, S. Wang, G. Buticchi, V. Varvolik, M. Galea, S. Bozhko, "Modulated model predictive speed controller for PMSM drives employing voltage-based cost function," *IEEE Open Journal of the Industrial Electronics Society*, vol. 5, pp. 122–131, 2024. **DOI:** 10.1109/OJIES.2024.3368568.

[12]. S. Mondal, P. Roy, A. Banerjee, U. Mondal, "A CKF-based sensor-less FOC integrated with gh-SVPWM for PMSM drives," *Electrical Engineering*, vol. 106, pp. 3461–3473, 2024. **DOI**: 10.1007/s00202-023-02169-8.

[13]. M. Nicola, C.-I. Nicola, "Improvement of linear and nonlinear control for PMSM using computational intelligence and reinforcement learning," *Mathematics*, vol. 10, no. 17, p. 3084, 2022. **DOI**: 10.3390/math10244667

[14]. Z. J. Jin, X. D. Sun, G. Lei, Y. G. Guo, J. G. Zhu, "Sliding mode direct torque control of SPMSMs based on a hybrid wolf optimization algorithm," *IEEE Transactions on Industrial Electronics*, vol. 69, no. 5, pp. 4534–4544, 2022. **DOI:** 10.1109/TIE.2021.3080220

[15]. S. Chen, W. Ding, R. Hu, X. Wu, S. Shi, "Sensorless control of PMSM drives using reduced order quasi resonant-based ESO and Newton Raphson method-based PLL," *IEEE Transactions on Power Electronics*, vol. 38, no. 1, pp. 229–244, 2023. **DOI:** 10.1109/TPEL.2022.3199773

[16]. Z. Wu, Z. Yang, K. Ding, G. He, "Transfer mechanism analysis of injected voltage harmonic and its effect on current harmonic regulation in FOC PMSM," *IEEE Transactions on Power Electronics*, vol. 37, no. 1, pp. 820–829, 2022. **DOI:** 10.1109/TPEL.2021.3097103

[17]. S. Wang et al., "Flux observer based on enhanced second-order generalized integrator with limit cycle oscillator for sensorless PMSM drives," *IEEE Transactions on Power Electronics*, vol. 38, no. 12, pp. 15982–15995, 2023. **DOI:** 10.1109/TPEL.2023.3314009

[18]. X. Sun, Y. Zhang, X. Tian, J. Cao, J. Zhu, "Speed sensorless control for IPMSMs using a modified MRAS with gray wolf optimization algorithm," *IEEE Transactions on Transportation Electrification*, vol. 8, no. 1, pp. 1326–1337, 2022. **DOI:** 10.1109/TTE.2021.3093580

[19]. Y. Zuo, C. Lai, K. L. V. Iyer, "A review of sliding mode observer based sensorless control methods for PMSM drive," *IEEE Transactions on Power Electronics*, vol. 38, no. 9, pp. 11352–11367, 2023. **DOI:** 10.1109/TPEL.2023.3287828

[20]. C. Dufour, S. Cense, J. Bélanger, "An induction machine and power electronic test system on a field-

programmable gate array," *Mathematics and Computers in Simulation*, vol. 130, pp. 112–123, 2016. DOI: 10.1016/j.matcom.2016.03.014

[21]. H. Yang, R. Yang, W. Hu, Z. Huang, "FPGA-based sensorless speed control of PMSM using enhanced performance controller based on the reduced-order EKF," *IEEE Journal of Emerging and Selected Topics in Power Electronics*, vol. 9, no. 1, pp. 289–301, 2021. **DOI:** 10.1109/JESTPE.2019.2962697

[22]. S. Gdaim, A. Mtibaa, M. F. Mimouni, "Artificial neural network-based DTC of an induction machine with experimental implementation on FPGA," *Engineering Applications of Artificial Intelligence*, vol. 121, p. 105972, 2023. **DOI:** 10.1016/j.engappai.2023.105972

[23]. N. R. Tavana, V. Dinavahi, "Real-time nonlinear magnetic equivalent circuit model of induction machine on FPGA for hardware-in-the-loop simulation," *IEEE Transactions on Energy Conversion*, vol. 31, no. 2, pp. 520–530, 2016. **DOI:** 10.1109/TEC.2015.2514099

[24]. A. Hasanzadeh, C. S. Edrington, N. Stroupe, T. Bevis, "Real-time emulation of a high-speed microturbine permanent-magnet synchronous generator using multiplatform hardware-in-the-loop realization," *IEEE Transactions on Industrial Electronics*, vol. 61, no. 6, pp. 3109–3118, 2014. **DOI**: 10.1109/TIE.2013.2279128